Advances in Aircraft and Spacecraft Science, *Vol. 12, No. 4 (2025) 347-366*
https://doi.org/10.12989/aas.2025.12.4.347

Dynamic analysis of graphene platelet-reinforced cylindrical shells subject to moving loads incorporating spinning effects

Qiong Shi[1], Wu-Bin Shan*[1], Huan Li[2] and Nan-Nan Zhang[1]

[1]*Hunan Electrical College of Technology, 411101, Xiangtan, PR China*
[2]*Changsha Environmental Protection College, Changsha, 410004, PR China*

(Received August 26, 2025, Revised September 29, 2025, Accepted October 13, 2025)

Abstract. Traditional analyses of cylindrical shells often neglect spinning motion, treating them as static/quasi-static structures, which leads to deviations in vibration, stress, and stability assessments. Current research on moving load-induced vibrations also overlooks spin rotation effects. This study investigates the time-dependent nonlinear dynamics of graphene-enhanced metal foam cylindrical shells (GPLRMF) with spinning motion. Using the first-order shear deformation theory and Galerkin's method for discretization, we develop an analytical framework validated via comparative analyses and convergence checks. Numerical integration (Runge-Kutta method) reveals a counterintuitive phenomenon: increasing spin rotation reduces vibration amplitudes. The study systematically evaluates spin motion, geometric imperfections, and other parameters, providing design guidelines for rotating shells under transient loading.

Keywords: cylindrical shells; geometric imperfection; spinning motion; thermal environment

1. Introduction

The spinning motion plays a significant role in the dynamic analysis of cylindrical shells, particularly under high-speed rotation or transient loading conditions. Traditional analyses often treat cylindrical shells as static or quasi-static structures, neglecting the effects of spinning motion, which leads to deviations in assessing vibration responses, stress distributions, and stability in practical engineering applications (Abouelregal 2022, 2024, Mohamed *et al.* 2024, Alibakhshi 2024, Cheng and She 2025). Spinning motion introduces Coriolis and centrifugal forces, significantly altering the nonlinear dynamic characteristics of the shell, such as inducing modal coupling, frequency shifts, and even instability phenomena. In advanced composite cylindrical shells like GPLRMF, the coupling effects of spinning motion with material anisotropy and geometric imperfections further complicate the analysis, necessitating high-order theories and numerical methods for accurate modeling (Goudarzfallahi *et al.* 2025, Civalek and Akgoz 2025, Fan and She 2026, Fan *et al.* 2025). Therefore, incorporating spinning motion analysis is critical for enhancing the reliability of rotating shell designs, especially for lightweight components in aerospace, high-speed machinery, and other fields. Recent studies have advanced the understanding of spinning cylindrical shells under diverse loading conditions. Monajemi *et al.*

*Corresponding author, Ph.D., E-mail: shanwubin2020@163.com

 ISSN: 2287-528X (Print), 2287-5271 (Online)

(2024) employed the differential quadrature method to analyze the thermomechanical responses of nanocomposite sandwich shells with magnetorheological elastomer cores, accounting for residual stresses. Zhang *et al.* (2024a) explored free vibrations of thermally loaded functionally graded stepped cylindrical shells under general boundary conditions using artificial springs. Meanwhile, Zhang *et al.* (2024b) developed a semi-analytical approach, combining the Gegenbauer-Ritz and state-space methods, to study wave propagation in GPLRMF stepped shells with discontinuous boundaries. Further contributions include Zhao *et al.* (2024), who modeled internal beam-attached graphene-reinforced shells, and Zhao *et al.* (2023), who numerically analyzed blade-coupled spinning drums. Liu *et al.* (2023) combined experiments with Donnell's theory to study elastic-boundary spinning shells, while Chai *et al.* (2023) proposed a semi-analytical frequency-response method using reduced eigenvectors. Teng and Wang (2023) derived critical speed equations for variable-thickness shells via Love's theory and Rayleigh-Ritz analysis. Finally, Dong *et al.* (2022) examined harmonic resonance in graded graphene-reinforced shells under thermal/external loads using Airy stress functions.

The moving load problem in cylindrical shell structures involves dynamic loads that vary with time (e.g., radial loads from rotating machinery or wheel loads from moving vehicles). A key feature is the continuous movement of load application points, which induces dynamic structural responses, causing stress concentrations, amplified vibrations, and potential buckling instability. This issue is crucial for engineering safety—for example, rotating loads on high-speed train axles require dynamic analysis to predict fatigue life, while bridges and tower structures must evaluate deformation and load-bearing capacity under moving loads. Optimal design must also consider thermo-mechanical coupling effects and material fatigue resistance. Numerous studies have explored the dynamic behavior of cylindrical shells under moving loads. Sheng and Wang (2009) developed coupling equations for functionally graded cylindrical shells with surface-bonded PZT piezoelectric layers under moving loads. Sofiyev (2010) conducted an analytical study on the dynamic behavior of infinitely long FGM cylindrical shells subjected to axial tension, internal compressive loads, and ring-shaped compressive pressure at constant velocity. Sofiyev *et al.* (2011) extended this analysis to non-homogenous orthotropic cylindrical shells on elastic foundations under similar loads. More recent research includes Mirjavadi *et al.* (2019), who analyzed the dynamic characteristics of functionally graded metal foam micro-scale shells in contact with moving loads, accounting for strain-gradient size-dependency. Eyvazian *et al.* (2020) studied FG-GNPRC cylindrical nanoshells under moving harmonic loads, varying load velocity and time history. Gao *et al.* (2024) proposed a stochastic vibration system for stepped composite cylindrical shells with drop-off plies under moving loads, using the pseudo excitation method. Li and She (2025) investigated the nonlinear transient response of graphene platelet-reinforced metal foam cylindrical shells under moving loads, considering initial geometric imperfections via the Runge-Kutta method. Li *et al.* (2025) examined stochastic vibration behaviors of functionally graded graphene platelet-reinforced composite joined conical-cylindrical-conical shells under moving random loads, employing the differential quadrature finite element method, pseudo excitation method, and Newmark-beta method. Zhang *et al.* (2023) investigated the nonlinear temperature-dependent dynamic behavior of a porous FG-GPLRC cylindrical panel under moving distributed loads, employing the Newmark direct integration method coupled with Newton-Raphson iteration. Meanwhile, Mirzaei and Abbasi (2023) examined the dynamic response of moderately thick graphene-reinforced composite cylindrical panels subjected to moving loads, utilizing the Ritz method with Chebyshev polynomial-based shape functions. Jafari and Kiani (2022b) performed the analysis of arbitrary thick graphene platelet reinforced composite plates

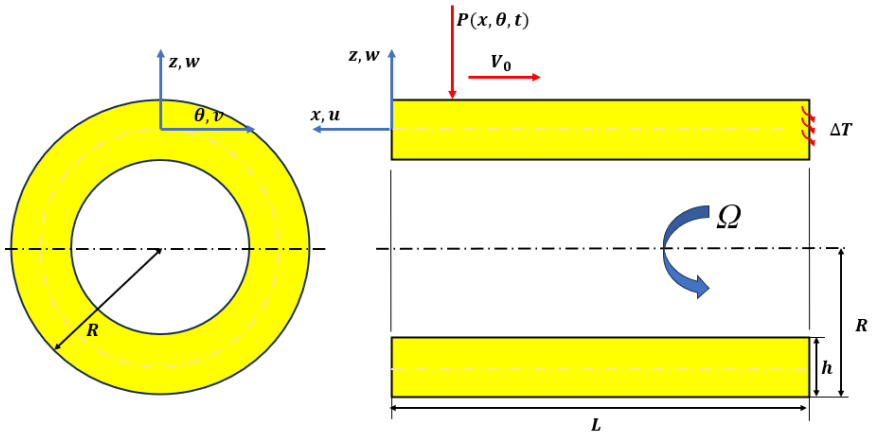

Fig. 1 A conceptual diagram of rotating cylindrical shell structure under moving load

subjected to moving load using a normal deformable plate model.

A comprehensive literature review reveals a critical research gap: the coupled effects of rotational dynamics and moving-load-induced vibrations on cylindrical shell structures remain unexplored. Specifically, no existing studies have investigated the dynamic behavior of self-spinning cylindrical shells under moving loads. To address this deficiency, this study pioneers an investigation into the time-domain response of simply supported cylindrical shells subjected to concurrent moving loads and rotational motions, considering non-uniform temperature fields. The numerical solutions obtained through fourth-order Runge-Kutta integration unveil novel mechanisms in this multi-physics interaction, establishing foundational theoretical principles for designing such systems.

2. Heat conduction to the temperature field

For the calculation of temperature fields in plate-shell structures, besides uniform temperature distributions, some scholars have proposed linear temperature distributions (Zhao *et al.* 2025). They assume that the temperature at each point within the structure varies linearly along the direction of the temperature gradient. However, these models do not account for heat conduction within the material and deviate from actual conditions. In this study, the inner and outer surface temperatures of the graphene-reinforced composite cylindrical shell are denoted as T_i and T_0, respectively, as shown in Fig. 1. Considering one-dimensional steady-state heat conduction along the shell thickness direction, the temperature field is defined as $T(z)=\tilde{T}+\Delta T$, where $\tilde{T}$ represents the initial temperature corresponding to the strain-free state of the composite cylindrical shell (which is set 300 K in this paper). According to Fourier's law of heat conduction, the heat flux q_z satisfies the following relationship with the temperature field (Dong *et al.* 2022)

$$q_z = -k_c(z)\frac{dT(z)}{dz} \tag{1}$$

According to the one-dimensional steady-state heat balance equation, the derivative of q_z with respect to z is equal to zero. Therefore, it can be obtained that (Ebrahimi and Salari 2015)

$$\frac{\mathrm{d}}{dz}\left(-k_c(z)\frac{dT(z)}{dz}\right)=0 \tag{2}$$

By integrating Eq. (2) twice from the lower limit $-h/2$ to the upper limit $h/2$, the one-dimensional steady-state temperature field along the thickness direction of the cylindrical shell is obtained

$$T(z)=c_1\int_{-h/2}^{z}\frac{1}{k_c(\eta)}\mathrm{d}\eta+c_2 \tag{3}$$

Where c_1 and c_2 are undetermined constants determined by the heat conduction boundary conditions. In this study, the temperature field of the cylindrical shell conforms to Dirichlet boundary conditions (Kiani and Eslami 2013)

$$T=T_i, z=h/2; T=T_0, z=-h/2. \tag{4}$$

Substitution of Eq. (4) into Eq. (3) determines the integration constants

$$c_1=\frac{(T_0-T_i)}{\int_{-h/2}^{h/2}\frac{1}{k_c(\eta)}\mathrm{d}\eta}, c_2=0. \tag{5}$$

Substituting Eq. (5) into Eq. (3) yields the temperature variation along the thickness direction of the cylindrical shell structure.

$$\Delta T(z)=\frac{(T_0-T_i)}{\int_{-h/2}^{h/2}\frac{1}{k_c(\eta)}\mathrm{d}\eta}\int_{-h/2}^{z}\frac{1}{k_c(\eta)}\mathrm{d}\eta+T_i-\hat{T} \tag{6}$$

3. Establishment and solution of the dynamic model

The geometric configuration of the GPLMF cylindrical shell is illustrated in Fig. 1, with L, R, and h denoting its axial length, mid-surface radius, and wall thickness, respectively. A constant-magnitude moving load P_0 traverses the shell surface at uniform velocity V_0 along a path parallel to the longitudinal axis. The effective material properties—including elastic modulus $E(z)$, density $\rho(z)$, thermal expansion coefficient $\alpha(z)$, and Poisson's ratio $\mu(z)$ —are mathematically characterized as per Refs. (Rafiee *et al.* 2009, Meksi *et al.* 2025, Esmaeili and Kiani 2022, Jafari and Kiani 2022a, Javani *et al.* 2021, 2022, Kiani and Mirzaei 2019, Wang and Kiani 2022),

$$\begin{bmatrix}E(z)\\ \rho(z)\\ \alpha(z)\\ \mu(z)\end{bmatrix}=\begin{bmatrix}\left[1-e_k\Gamma_k(z)\right]\left\{\frac{3}{8}\left(\frac{1+\zeta_l\eta_lV_{gpl}}{1-\eta_lV_{gpl}}\right)E_m+\frac{5}{8}\left(\frac{1+\zeta_w\eta_wV_{gpl}}{1-\eta_wV_{gpl}}\right)E_m\right\}\\ \left[1-e_{mk}\Gamma_k(z)\right]\left(\rho_{gpl}V_{gpl}+\rho_mV_m\right)\\ \alpha_{gpl}V_{gpl}+\alpha_mV_m\\ \mu_{gpl}V_{gpl}+\mu_mV_m\end{bmatrix} \tag{7}$$

in which, $\zeta_l = \frac{2l_{gpl}}{t_{gpl}}, \zeta_{w=} \frac{2w_{gpl}}{t_{gpl}}, \eta_l = \frac{E_{gpl} - E_m}{E_{gpl} + \zeta_l E_m}, \eta_w = \frac{E_{gpl} - E_m}{E_{gpl} + \zeta_w E_m}$. The material coefficients governing the functionally graded foam structure are systematically defined as follows: e_k (where $k \in [1,2,3]$) characterizes the porosity distribution gradient, while e_{mk} quantifies the corresponding mass density variation. The constituent material parameters are distinctly categorized into two groups: *gpl* represents the geometric and physical properties of graphene platelets (GPLs), and m denotes the metallic matrix properties. Specifically, the superscripted variables l_{gpl}, w_{gpl}, and t_{gpl} correspond to the characteristic dimensions (length, width, and thickness) of the GPL reinforcements (Zhang *et al.* 2025, Salehi *et al.* 2023)

$$\Gamma_k(z) = \begin{cases} \cos(\pi z / h) & (\text{Foam - I}) \\ 1 - \cos(\pi z / h) & (\text{Foam - II}) \\ 1 & (\text{Foam - III}) \end{cases} \tag{8}$$

For this shell, the functional interdependence between porosity parameters (e_k) and density variation coefficients (e_{mk}) is mathematically described by (Zhao and She 2025),

$$\begin{cases} 1 - e_{m1}\Gamma_1(z) = \sqrt{1 - e_1\Gamma_1(z)} \\ 1 - e_{m2}\Gamma_2(z) = \sqrt{1 - e_2\Gamma_2(z)} \\ e_{m3} = \sqrt{e_3} \end{cases} \tag{9}$$

Under the condition of constant total graphene platelets (GPLs) content, the porosity coefficient e_k can be mathematically derived through the following constitutive relation

$$\int_0^{\frac{h}{2}} \sqrt{1 - e_1\Gamma_1(z)}dz = \int_0^{\frac{h}{2}} \sqrt{1 - e_2\Gamma_2(z)}dz = \int_0^{\frac{h}{2}} \sqrt{e_3}dz \tag{10}$$

Three distinct spatial dispersion patterns of graphene platelets (GPLs) exhibit characteristic volume concentration profiles, specifically (Li and She 2025, Cheng *et al.* 2025)

$$V_{GPL} = \begin{cases} Si_1\Gamma_2(z), & (\text{GPL-A}) \\ Si_2\Gamma_1(z), & (\text{GPL-B}) \\ Si_3, & (\text{GPL-C}) \end{cases} \tag{11}$$

The dimensionless coefficients Si_1, Si_2, and Si_3 in Eq. (5) are derived from the dimensionless analysis of Refs. (Li and She 2025).

Within the framework of FSDT, the kinematic field variables are expressed through five independent displacement components, comprising (Li and She 2025)

$$\begin{aligned} u_x(x,\theta,z,t) &= u_0(x,\theta,t) + z\varphi_x(x,\theta,t) \\ u_\theta(x,\theta,z,t) &= v_0(x,\theta,t) + z\varphi_\theta(x,\theta,t) \\ u_z(x,\theta,z,t) &= w_0(x,\theta,t) + w_1(x,\theta) \end{aligned} \tag{12}$$

The displacement field components (u_0, v_0, w_0) correspond to the axial, hoop, and through-thickness directions of the cylindrical coordinate system, while (φ_x, φ_θ) represent the rotational

degrees of freedom about the respective axes. The initial geometric deviation from perfect cylindrical form, characterized by the deflection component $w_1=\sum_{m=1}^{\infty}\sum_{n=1}^{\infty}W_1\sin\left(\frac{m\pi x}{L}\right)\sin(n\theta)$, is incorporated to account for manufacturing tolerances. The finite strain-displacement relationships are formulated under von Kármán's assumptions for moderate rotations (Baakeel *et al.* 2023), where the second-order terms of displacement gradients are retained in the Green-Lagrange strain tensor components

$$\begin{bmatrix}\varepsilon_{xx}\\ \varepsilon_{\theta\theta}\\ \varepsilon_{x\theta}\\ \gamma_{xz}\\ \gamma_{\theta z}\end{bmatrix}=\begin{bmatrix}\dfrac{\partial u_0}{\partial x}+\dfrac{1}{2}\left(\dfrac{\partial(w_0+w_1)}{\partial x}\right)^2\\ \dfrac{1}{R}\dfrac{\partial v_0}{\partial\theta}+\dfrac{(w_0+w_1)}{R}+\dfrac{1}{2R^2}\left(\dfrac{\partial(w_0+w_1)}{\partial\theta}\right)^2\\ \dfrac{1}{R}\dfrac{\partial u_0}{\partial\theta}+\dfrac{\partial v_0}{\partial x}+\dfrac{1}{R}\dfrac{\partial(w_0+w_1)}{\partial x}\dfrac{\partial(w_0+w_1)}{\partial\theta}\\ \varphi_x+\dfrac{\partial(w_0+w_1)}{\partial x}\\ \varphi_\theta+\dfrac{1}{R}\dfrac{\partial(w_0+w_1)}{\partial\theta}\end{bmatrix}+z\begin{bmatrix}\dfrac{\partial\varphi_x}{\partial x}\\ \dfrac{1}{R}\dfrac{\partial\varphi_\theta}{\partial\theta}\\ \dfrac{1}{R}\dfrac{\partial\varphi_x}{\partial\theta}+\dfrac{\partial\varphi_\theta}{\partial x}\end{bmatrix} \tag{13}$$

The coupled thermoelastic constitutive equations, accounting for finite temperature variations, expressed by

$$\begin{bmatrix}\sigma_{xx}\\ \sigma_{\theta\theta}\\ \sigma_{x\theta}\\ \sigma_{xz}\\ \sigma_{\theta z}\end{bmatrix}=\begin{bmatrix}Q_{11}&Q_{12}&0&0&0\\ Q_{12}&Q_{22}&0&0&0\\ 0&0&Q_{66}&0&0\\ 0&0&0&\frac{5}{6}Q_{55}&0\\ 0&0&0&0&\frac{5}{6}Q_{44}\end{bmatrix} \times\left[\begin{Bmatrix}\varepsilon_{xx}\\ \varepsilon_{\theta\theta}\\ \varepsilon_{x\theta}\\ \gamma_{xz}\\ \gamma_{\theta z}\end{Bmatrix}-\frac{(T_0-T_i)}{\int_{-h/2}^{h/2}\frac{1}{k_c(\eta)}\mathrm{d}\eta}\int_{-h/2}^{z}\frac{1}{k_c(\eta)}\mathrm{d}\eta+T_i-\hat{T}\begin{Bmatrix}\alpha(z)\\ \alpha(z)\\ 0\\ 0\\ 0\end{Bmatrix}\right] \tag{14}$$

Herein, $Q_{11}=Q_{22}=\dfrac{E(z)}{1-\mu(z)^2}$, $Q_{12}=\dfrac{vE(z)}{1-\mu(z)^2}$, $Q_{66}=\dfrac{E(z)}{2(1+\mu(z))}$, $Q_{44}=Q_{55}=Q_{66}$.

The governing equations of motion are obtained through application of Hamilton's variational principle, where the stationarity condition $\int_{t_1}^{t_2}(\delta\Upsilon_k-\delta\Upsilon_u+\delta\Upsilon_w)dt=0$ is imposed on the total energy functional Π comprising kinetic energy $\delta\Upsilon_k$, potential energy Υ_u, and external work Υ_w over the time domain [t_1, t_2], with

$$\Upsilon_k = \frac{1}{2}\int_0^L\int_0^{2\pi}\int_{-h/2}^{h/2}\left[\rho(z)\left\{\left[\frac{\partial u_0}{\partial t}+\frac{z\partial\varphi_x}{\partial t}\right]^2+\left[\frac{\partial v_0}{\partial t}+z\frac{\partial\varphi_\theta}{\partial t}\right]^2+\left[\frac{\partial(w_0+w_1)}{\partial t}\right]^2\right\}\right.$$
$$+2\Omega\left(u_z\left[\frac{\partial v_0(x,\theta,t)}{\partial t}+z\frac{\partial\varphi_\theta(x,\theta,t)}{\partial t}\right]-u_\theta\left[\frac{\partial(w_0+w_1)}{\partial t}\right]\right) \tag{15}$$
$$\left.+\Omega^2\left(\left[\frac{\partial v_0}{\partial t}+z\frac{\partial\varphi_\theta}{\partial t}\right]^2+\left[\frac{\partial(w_0+w_1)}{\partial t}\right]^2\right)\right]rdzd\theta dx$$

$$\Upsilon_u = \frac{1}{2}\int_0^L\int_0^{2\pi}\int_{-h/2}^{h/2}\left(\sigma_{xx}\varepsilon_{xx}+\sigma_{\theta\theta}\varepsilon_{\theta\theta}+\sigma_{x\theta}\varepsilon_{x\theta}+\sigma_{xz}\gamma_{xz}+\sigma_{\theta z}\gamma_{\theta z}\right)rdzd\theta dx$$
$$+\frac{1}{2}\int_0^L\int_0^{2\pi}\int_{-h/2}^{h/2}\rho(z)r^2\Omega^2\left\{\frac{1}{r^2}\left[\left(\frac{\partial u_x}{\partial\theta}\right)^2+\left(\frac{\partial u_y}{\partial\theta}+u_z\right)^2+\left(u_y-\frac{\partial u_z}{\partial\theta}\right)^2\right]\right\}rdzd\theta dx \tag{16}$$

$$\Upsilon_w = -\int_0^L\int_0^{2\pi}p(x,\theta,t)\,w_0 rd\theta dx-\int_0^{2\pi}C_t\frac{\partial(w_0+w_1)}{\partial t}\delta w r dx d\theta \tag{17}$$

The governing vibration Eqs. (15)-(17) incorporate three characteristic parameters: C_t - viscous damping coefficient of the system. The governing dynamic equations are systematically derived through substitution of the constitutive relations (15)-(17) into the fundamental equilibrium equation $\int_{t_1}^{t_2}\left(\delta\Upsilon_k-\delta\Upsilon_u+\delta\Upsilon_w\right)dt=0$, resulting in the complete coupled system

$$\frac{\partial N_{xx}}{\partial x}+\frac{1}{r}\frac{\partial N_{x\theta}}{\partial\theta}=I_0\frac{\partial^2 u_0}{\partial t^2}+I_1\frac{\partial^2\varphi_x}{\partial t^2}-\Omega^2\left(I_0\frac{\partial^2 u_0}{\partial\theta^2}+I_1\frac{\partial^2\varphi_x}{\partial\theta^2}\right) \tag{18}$$

$$\frac{1}{r}\frac{\partial N_{\theta\theta}}{\partial\theta}+\frac{\partial N_{x\theta}}{\partial x}=I_0\frac{\partial^2 v_0}{\partial t^2}+I_1\frac{\partial^2\varphi_\theta}{\partial t^2}-\Omega^2\left(I_0\frac{\partial^2 v_0}{\partial\theta^2}+I_1\frac{\partial^2\varphi_\theta}{\partial\theta^2}+2I_0\frac{\partial(w_0+w_1)}{\partial\theta}\right)+2\Omega I_0\frac{\partial w_0}{\partial t} \tag{19}$$

$$\frac{\partial N_{xz}}{\partial x}+\frac{1}{r}\frac{\partial N_{\theta z}}{\partial\theta}-\frac{1}{r}N_{\theta\theta}+\hat{N}-p(x,\theta,t)=I_0\frac{\partial^2(w_0+w_1)}{\partial t^2}-2\Omega\left(I_0\frac{\partial v_0}{\partial t}+I_1\frac{\partial\varphi_0}{\partial t}\right)$$
$$-\Omega^2\left[I_0\frac{\partial^2(w_0+w_1)}{\partial\theta^2}-2\left(I_0\frac{\partial v_0}{\partial\theta}+I_1\frac{\partial\varphi_\theta}{\partial\theta}\right)\right] \tag{20}$$

$$\frac{\partial M_{xx}}{\partial x}+\frac{1}{r}\frac{\partial M_{x\theta}}{\partial\theta}-N_{xz}=I_0\frac{\partial^2 u_0}{\partial t^2}+I_2\frac{\partial^2\varphi_x}{\partial t^2}-\Omega^2\left(I_1\frac{\partial^2 u_0}{\partial\theta^2}+I_2\frac{\partial^2\varphi_x}{\partial\theta^2}\right) \tag{21}$$

$$\frac{1}{r}\frac{\partial M_{\theta\theta}}{\partial\theta}+\frac{\partial M_{x\theta}}{\partial x}-N_{\theta z}=I_0\frac{\partial^2 v_0}{\partial t^2}+I_2\frac{\partial^2\varphi_x}{\partial t^2}+2\Omega I_1\frac{\partial(w_0+w_1)}{\partial t}$$
$$-\Omega^2\left(I_1\frac{\partial^2 v_0}{\partial\theta^2}+2I_1\frac{\partial(w_0+w_1)}{\partial\theta}+I_2\frac{\partial^2\varphi_\theta}{\partial\theta^2}\right) \tag{22}$$

where, $\hat{N}$ represents the nonlinear term, $\{I_0, I_1, I_2\} = \int_{-h/2}^{h/2} \rho(z)\{1, z, z^2\}\,\mathrm{d}z$, and

$$\begin{aligned}
&\{N_{ij}, M_{ij}\} = \int_{-h/2}^{h/2} \sigma_{ij}\{1, z\}\,\mathrm{d}z, (i, j) = (x, \theta, z),\\
&\hat{N} = \frac{1}{r}\left[\left(rN_{xx}\frac{\partial(w_0 + w_1)}{\partial x} + N_{x\theta}\frac{\partial(w_0 + w_1)}{\partial \theta}\right) + \frac{\partial}{\partial \theta}\left(\frac{1}{r}N_{\theta\theta}\frac{\partial(w_0 + w_1)}{\partial \theta} + N_{x\theta}\frac{\partial(w_0 + w_1)}{\partial x}\right)\right].
\end{aligned} \tag{23}$$

Assuming the solution of Eq. (23) can be expressed in the following trigonometric series form, its solution satisfying simply-supported boundary conditions may be represented as (Li and She 2025)

$$\begin{aligned}
u_0 &= \sum_{m=1}^{M}\sum_{n=1}^{N} U_{mn}(t)\cos(\frac{m\pi x}{L})\sin(n\theta) = \boldsymbol{\xi}_u{}^{\mathrm{T}}\mathbf{U},\\
v_0 &= \sum_{m=1}^{M}\sum_{n=1}^{N} V_{mn}(t)\sin(\frac{m\pi x}{L})\cos(n\theta) = \boldsymbol{\xi}_v{}^{\mathrm{T}}\mathbf{V},\\
w_0 &= \sum_{m=1}^{M}\sum_{n=1}^{N} W_{mn}(t)\sin(\frac{m\pi x}{L})\sin(n\theta) = \boldsymbol{\xi}_w{}^{\mathrm{T}}\mathbf{W},\\
\varphi_x &= \sum_{m=1}^{M}\sum_{n=1}^{N} \Phi_{mn}(t)\cos(\frac{m\pi x}{L})\sin(n\theta) = \boldsymbol{\xi}_{\varphi_x}{}^{\mathrm{T}}\boldsymbol{\Phi},\\
\varphi_y &= \sum_{m=1}^{M}\sum_{n=1}^{N} \Psi_{mn}(t)\sin(\frac{m\pi x}{L})\cos(n\theta) = \boldsymbol{\xi}_{\varphi_y}{}^{\mathrm{T}}\boldsymbol{\Psi}.
\end{aligned} \tag{24}$$

The modal decomposition expresses dynamic responses through time-dependent coefficients: $U_{mn}(t)$, $V_{mn}(t)$, $W_{mn}(t)$- Temporal amplitudes for in-plane and transverse displacements; $\Phi_{xmn}(t)$, $\Phi_{ymn}(t)$-Rotational component modulations, where integers (m,n) denote spatial half-wavelength counts. These collectively form the generalized coordinate space: $\mathbf{U}=[U_{mn}]$, $\mathbf{V}=[V_{mn}]$, $\mathbf{W}=[W_{mn}]$, $\boldsymbol{\Phi}=[\boldsymbol{\Phi}_{mn}]$, $\boldsymbol{\Psi}=[\Psi_{mn}]$ with corresponding characteristic basis functions $\boldsymbol{\xi_u}$, $\boldsymbol{\xi_v}$, $\boldsymbol{\xi_w}$ that satisfy the orthogonality conditions, as employed in Eq. (24)'s matrix formulation. Dynamic excitation propagating along the structure admits the functional representation (Eyvazian *et al.* 2020)

$$p(x, \theta, t) = \sum_{m=1}^{\infty}\sum_{n=1}^{\infty} P_{mn}(t)\sin\left(\frac{m\pi x}{L}\right)\cos(n\theta) \tag{25}$$

Herein, $P_{mn}(t) = \begin{cases} \dfrac{2P_0}{mn\pi RL}\sin(\dfrac{m\pi V_0 t}{L}) & t < t_f \\ 0 & t > t_f \end{cases}$, with $t_f = L/V_0$.

Applying Eq. (25) as trial functions to Eqs. (18)-(22) under Galerkin-weighted residuals yields

$$\mathbf{M}\ddot{\mathbf{q}} + \mathbf{K}_L\mathbf{q} + \mathbf{K}_{NL}(\mathbf{q}) = \mathbf{F} \tag{26}$$

The governing system employs the following matrix operators: $\mathbf{q} = \left[\mathbf{U}^T, \mathbf{V}^T, \mathbf{W}^T, \boldsymbol{\Phi}^T, \boldsymbol{\Psi}^T\right]^T$ - Column vector; **M**-Inertial mass matrix; $\mathbf{K_L}$-Linear elastic stiffness operator; $\mathbf{K_{NL}}$-Geometrically

nonlinear stiffness component, and $\mathbf{F}=\iint_A P_{mn}(t)\sin\left(\frac{m\pi x}{L}\right)\cos(n\theta)dA$. The state vectors (defined in Eq. (26)) collectively form the configuration space for this dynamical system. The governing parameters enable numerical integration of Eq. (26) through fourth-order Runge-Kutta iteration. The basic approach to solving such a complex equation is as follows, for the second-order linear ordinary differential equation

$$\begin{cases} \frac{\mathrm{d}^2\Upsilon}{d\chi^2}=f\left(\chi,\Upsilon,\frac{\mathrm{d}\Upsilon}{d\chi}\right) \\ \Upsilon(\chi_0)=\Upsilon_0 \\ \gamma'(\chi_0)=\Upsilon_0' \end{cases} \tag{27}$$

Herein, Υ is a function of χ， A prime (‘) denotes the derivative of the corresponding variable.

To reduce the above second-order ordinary differential equation to a first-order ordinary differential equation, we let

$$\begin{cases} \Upsilon_1=\Upsilon \\ \Upsilon_1(\chi_0)=\Upsilon_0 \\ \Upsilon_2=\frac{d\Upsilon}{d\chi} \\ \Upsilon_2(\chi_0)=\Upsilon_0' \end{cases} \tag{28}$$

Using Eq. (28), Eq. (27) becomes a first-order ordinary differential equation, given as

$$\begin{cases} \frac{\mathrm{d}\Upsilon_1}{d\chi}=\Upsilon_2 \\ \frac{\mathrm{d}\Upsilon_2}{d\chi}=f(\chi,\Upsilon_1,\Upsilon_2) \\ \Upsilon_1(\chi_0)=\Upsilon_0 \\ \Upsilon_2(\chi_0)=\Upsilon_0' \end{cases} \tag{29}$$

It should be noted that in the following calculations, the step size is chosen as 0.00001 seconds.

4. Numerical results

Table 1 enumerates the constitutive material properties employed in this study, with the dimensionless parameter Λ expressed analytically as

$$\mathrm{P}=P_0\left(\frac{P_{-1}}{T}+1+P_1T+P_2T^2+P_3T^3\right) \tag{30}$$

Table 1 Material properties (Dong *et al.* 2020)

Materials	Properties	P_{-1}	P_0	P_1	P_2	P_3
Nickel	E_m (Pa)	0	223.95×10^{9}	-2.974×10^{-4}	-3.998×10^{-9}	0
	μ_m	0	0.31	0	0	0
	ρ_m (kg/m^3)	0	8908	0	0	0
	α_m (1/K)	0	9.9209×10^{-6}	8.7056×10^{-4}	0	0
GPLs	E_{gpl} (Pa)	0	1087.8×10^{9}	-0.261×10^{9}	0	0
	μ_{gpl}	0	0.186	0	0	0
	ρ_{gpl} (kg/m^3)	0	1060	0	0	0
	α_{gpl} (1/K)	0	13.920×10^{-6}	-0.0299×10^{-6}	0	0

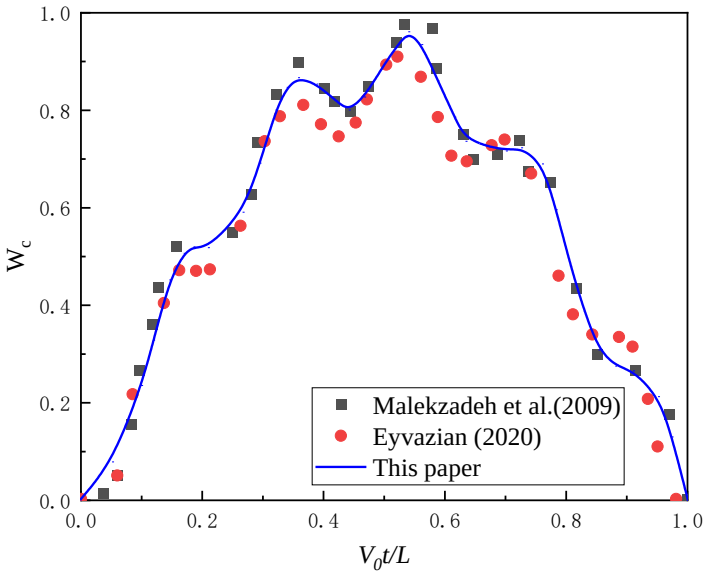

Fig. 2 Benchmark results for moving load-induced vibration characteristics of cylindrical shells (without spinning motion condition)

Under ambient temperature T, the graphene platelets (GPLs) exhibit the following nanoscale dimensions: l_{gpl}=2.5 um, w_{gpl}=1.5 um, h_{gpl}=1.5 nm. These dimensional parameters govern all subsequent computational analyses.

The computational framework is rigorously verified through comparative analysis in Fig. 2, where the moving load-induced dynamic responses of cylindrical shells demonstrate excellent consistency with differential quadrature solutions by Malekzadeh's team (2009) and state-space formulations from Eyvazian (2020). This cross-method validation establishes the numerical reliability of the proposed approach. The convergence behavior of the moving load-induced dynamic response is rigorously examined in Fig. 3 through normalized midpoint deflection analysis of a simply-supported cylindrical shell incorporating GPL-A reinforced Foam-II distribution. The dimensionless time (v_0t/L) and normalized central deflection (w_c) are respectively plotted along the horizontal and vertical axes, revealing distinct vibration regimes: forced vibration dominates when v_0t/L<1, while free vibration prevails beyond this critical transition point. Numerical stabilization is achieved at the truncation parameter combination of M=N=8, with

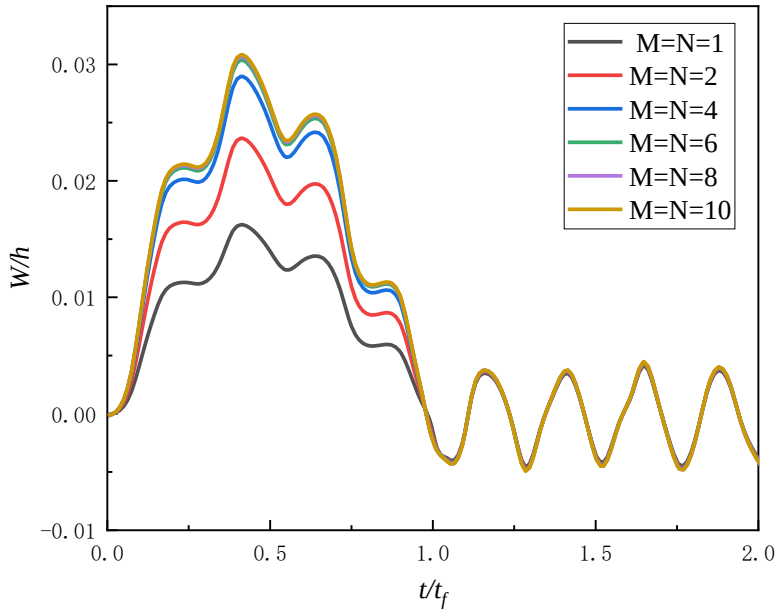

Fig. 3 Convergence verification (ΔT=100 K, e_1=0.1, W_1=0.1, V_0=240 m/s, P_0=6 Mpa, W_{gpl}=0.1%, Ω=500 rad/s)

further mesh refinement yielding negligible improvements. This computationally efficient configuration is consequently employed throughout subsequent parametric studies.

Fig. 4 shows the effect of material properties, and the parametric investigation presented in Fig. 4(a) systematically evaluates the dynamic performance variation induced by different graphene platelet (GPL) dispersion patterns in cylindrical shells subjected to combined mechanical and geometric constraints. Comparative analysis reveals that GPL-A configuration achieves 10.3% reduction in maximum dynamic deflection amplitude compared to GPL-B during forced vibration phase, establishing its superior reinforcement efficiency attributed to the concentrated GPLs distribution near shell surfaces. This stiffness enhancement mechanism, however, exhibits diminished dominance during free vibration regime where the amplitude advantage is no longer maintained, suggesting different optimization criteria may apply for transient versus steady-state responses.

The comparative analysis in Fig. 4(b) reveals significant variations in structural performance among three distinct foam core distribution configurations (Foam-I, Foam-II, Foam-III) for cylindrical shells containing 0.2% weight fraction of GPL reinforcement. Results demonstrate that Foam-I topology achieves 9.6% reduction in maximum central deflection compared to Foam-III distribution, with the mechanical advantage primarily stemming from its characteristic mid-plane foam concentration. This specific material architecture enhances flexural rigidity through optimized stress distribution across the shell thickness, whereas foam accumulation near inner/outer surfaces (characteristic of Foam-III) creates localized compliance zones that compromise structural integrity under dynamic loading. The fundamental stiffness-load capacity relationship established in this study validates Foam-I distribution as the optimal design configuration for applications requiring superior deflection resistance.

The parametric study presented in Fig. 4(c) quantitatively characterizes the sensitivity of

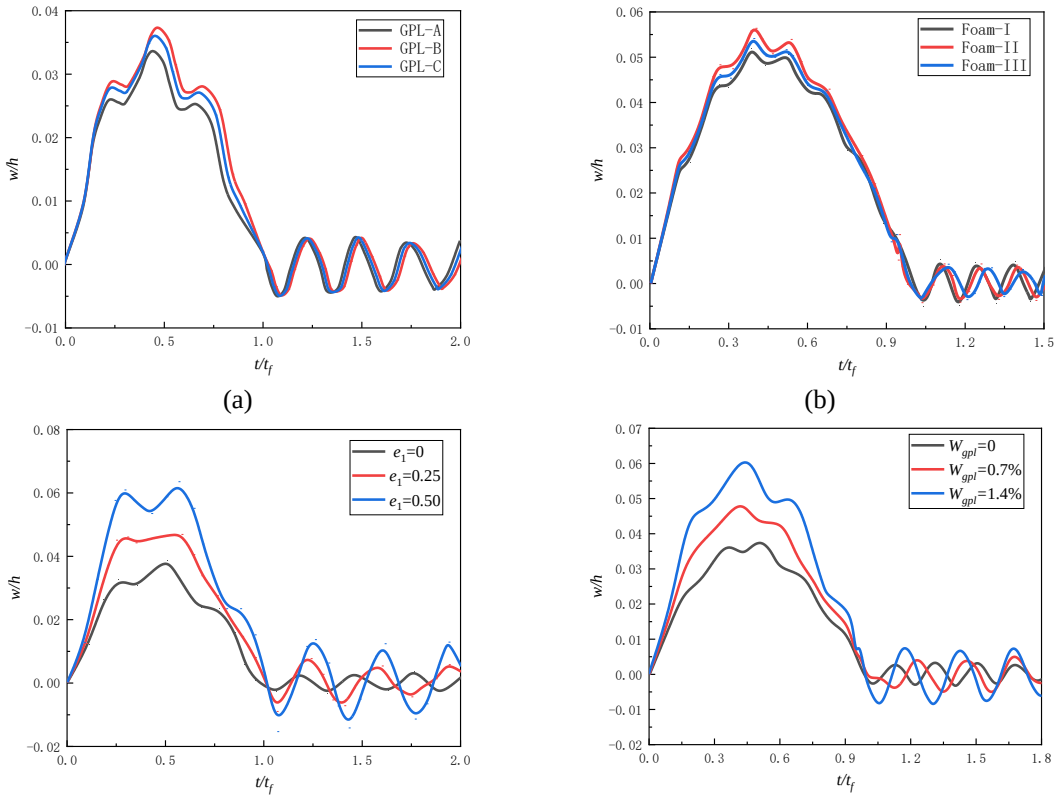

Fig. 4 Effect of material properties (a) Effect of GPLs distribution (ΔT=150 K, e_1=0.1, W_1=0.1, V_0=240 m/s, W_{gpl}=0.1%, Foam-II, h=0.4 m, L=R=2 m, Ω=500 rad/s); (b) Effect of foam distributions (ΔT=150 K, e_1=0.1, W_1=0.1, V_0=300 m/s, W_{gpl}=0.1%, h=0.4 m, L=R=2 m, GPL-A, Ω=500 rad/s); (c) Effect of foam coefficient (ΔT=150 K, Foam-II, W_1=0.1, V_0=300 m/s, W_{gpl}=0.1%, h=0.4 m, L=R=2 m, GPL-A, Ω=500 rad/s); (d) Effect of GPLs weight fractions (ΔT=150 K, Foam-II, W_1=0.1, V_0=240 m/s, e_1=0.2, h=0.4 m, L=R=2 m, GPL-A, Ω=500 rad/s)

structural response to foam coefficient (e_1) variations in GPL-reinforced cylindrical shells. As evidenced in Fig. 4(c), progressive escalation of e_1 from 0 to 0.25 and 0.50 induces respective deflection amplifications of 25.1% and 63.4% in the forced vibration range. This nonlinear stiffness degradation trend is even more pronounced in free vibration, where the same e_1 increments cause deflection increases of 180.4% and 422.4%. The mechanical softening phenomenon persists throughout the free vibration phase, with structures exhibiting higher e_1 values maintaining proportionally larger oscillation amplitudes - a direct consequence of reduced bending stiffness caused by foam-induced modulus reduction. The established e_1-deflection correlation provides critical design guidelines for balancing weight reduction objectives with load-bearing requirements in lightweight composite structures.

The parametric study in Fig. 4(d) systematically evaluates three discrete W_{GPL} weight fractions (0%, 0.7%, 1.4%) to quantify their reinforcement effects in rotating cylindrical shells. The results demonstrate an inverse correlation between GPL concentration and dynamic response amplitude: during forced vibration, the maximum central deflection decreases by 37.6% as W_{GPL} increases

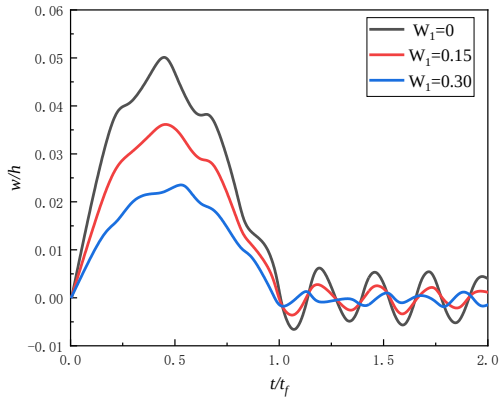

Fig. 5 Effect of initial geometric imperfection (ΔT=150 K, e_1=0.1, GPL-A, V_0=240 m/s, W_{gpl}=0.1%, Foam-II, h=0.4 m, L=R=2 m, Ω=500 rad/s)

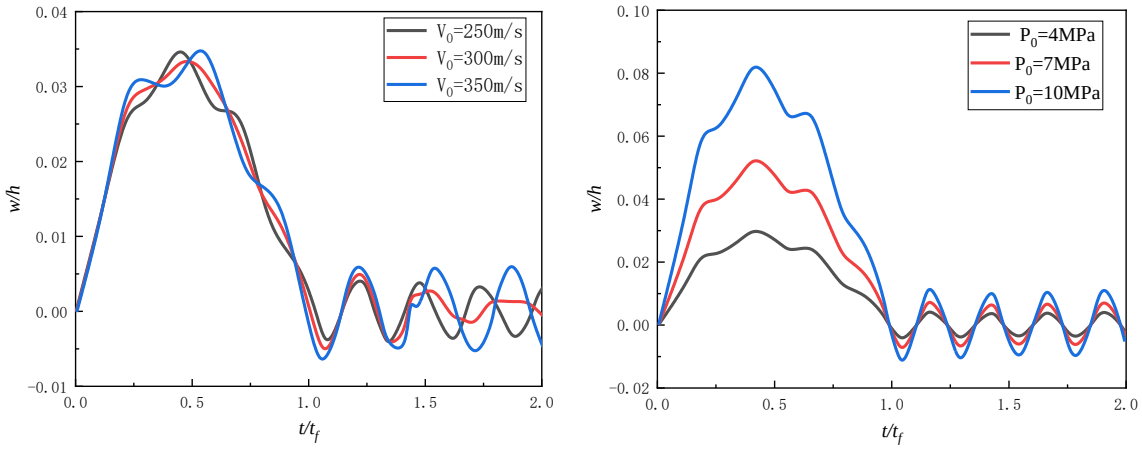

(a) (b)

Fig. 6 Effect of (a) load moving velocity (ΔT=150 K, e_1=0.1, GPL-A, W_{gpl}=0.1%, Foam-II, h=0.4 m, L=R=2 m, P_0=5 MPa, Ω=500 rad/s) and (b) load intensity (ΔT=150 K, e_1=0.1, GPL-A, V_0=240 m/s, W_{gpl}=0.1%, Foam-II, h=0.4 m, L=R=2 m, Ω=500 rad/s)

from 0% to 1.4%, while in free vibration, the deflection reduction reaches 65.4% with a simultaneous 4.9% contraction in oscillation period under the same conditions. This stiffness enhancement originates from the effective stress transfer at the nanofiller-matrix interface, which induces GPL-mediated modulus improvement. The combined findings confirm that the incorporation of GPL simultaneously enhances both static and dynamic load-bearing capacities through graphene mass fraction optimization.

The systematic investigation in Fig. 5 elucidates the counterintuitive mechanical response of graphene platelet-reinforced (GPL-A) cylindrical shells to controlled geometric imperfections (W_1 range of 0-0.2). Contrary to conventional expectations, the results demonstrate that progressively introducing initial imperfections significantly suppresses deflection: during forced vibration, the maximum central deflection decreases by 28.0% and 53.0% as W_1 increases from 0 to 0.15 and 0.30, respectively. This suppression effect is even more pronounced in free vibration, where the

same increments in W_1 cause deflection reductions of 56.0% and 80.2%. This anomalous behavior originates from imperfection-induced curvature alterations that fundamentally modify the shell's load transfer mechanism: (1) Enhanced contact area distribution through localized curvature amplification, and (2) Activated membrane stress redistribution that compensates for bending stiffness reduction. The established inverse W_1-deflection correlation provides new insights for leveraging controlled imperfections as a potential design parameter in energy-absorbing structural applications.

The systematic study in Fig. 6(a) demonstrates the influence of load moving velocity (V_0). As anticipated, the results show that progressively increasing the load moving velocity significantly amplifies deflection. During the forced vibration phase, the maximum central deflection increases by 3.4% and 3.8% as V_0 rises from 250 m/s to 300 m/s and 350 m/s, respectively. This effect becomes even more pronounced in the free vibration phase, where the same increments in V_0 cause deflection increases of 25.8% and 57.8%. This behavior arises from the fact that higher moving velocities induce greater structural damage. The observed velocity-dependent deflection amplification provides critical insights for evaluating high-speed impact scenarios and optimizing structural integrity under dynamic loading conditions.

The study presented in Fig. 6(b) investigates the influence of load intensity (P_0). As expected, the results demonstrate that progressively increasing the load intensity significantly amplifies deflection. During the forced vibration phase, the maximum central deflection increases by 77.8% and 177.1% as P_0 rises from 4 MPa to 7 MPa and 10 MPa, respectively. Similarly, in the free vibration phase, the same increments in P_0 cause deflection increases of 106.5% and 206.2%. This behavior stems from the fact that higher load intensity results in greater structural damage and impact force, which naturally leads to larger dynamic displacement responses. The observed load-intensity-dependent deflection amplification provides valuable insights for assessing structural behavior under varying loading conditions and optimizing design parameters for impact-resistant applications.

The systematic study in Fig. 7(a) investigates the dynamic response of moving loads under temperature variations (ΔT=0 K, 100 K, 200 K). As expected, the results demonstrate that progressively introducing temperature significantly suppresses deflection. During the forced vibration phase, the maximum central deflection decreases by 6.9% and 13.2% as ΔT increases from 0 to 100 K and 200 K, respectively. Similarly, in the free vibration phase, the same increments in ΔT cause deflection reductions of 12.9% and 23.9%. This behavior arises from the thermal expansion and thermal stress induced by temperature, fundamentally altering the thermal deformation of the cylindrical shell: (1) Thermal deformation amplifies dynamic displacement responses; (2) The activated thermal stress redistribution simultaneously reduces bending stiffness. The established negative correlation between temperature change and deflection provides new insights for controlling thermal deformation as a potential design parameter.

The systematic study presented in Fig. 7(b) investigates the dynamic response of moving loads under rotational speed variations ($\Delta\Omega$=0, 500 rad/s, 1000 rad/s). Contrary to conventional expectations, the results demonstrate that progressively introducing rotational speed significantly suppresses deflection. During the forced vibration phase, the maximum central deflection decreases by 1.6% and 22.3% as $\Delta\Omega$ increases from 0 to 500 rad/s and 1000 rad/s, respectively. Similarly, in the free vibration phase, the same increments in $\Delta\Omega$ cause deflection reductions of 10.5% and 30.2%. This behavior arises from the centrifugal force induced by rotational speed, which fundamentally counteracts the deformation of the cylindrical shell. The observed rotational speed-dependent deflection suppression provides valuable insights for optimizing structural design

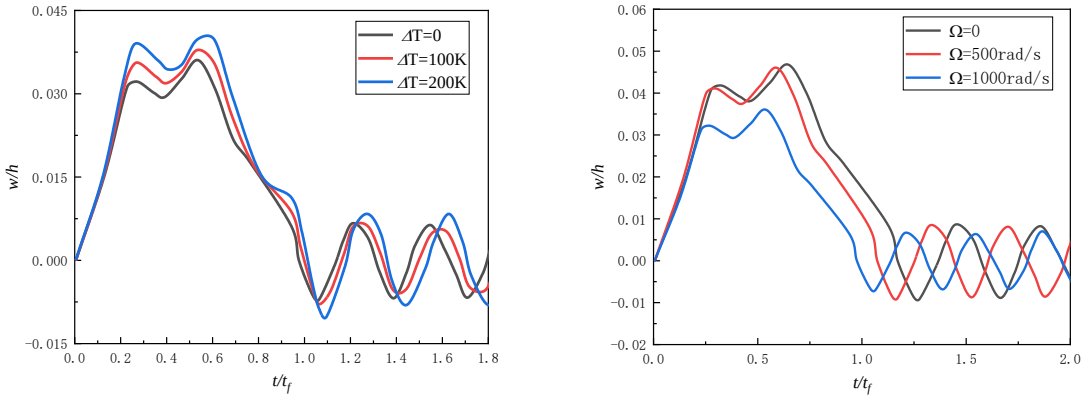

(a) (b)

Fig. 7 Effect of (a) temperature rise (W_1=0.1, e_1=0.1, GPL-A, V_0=240 m/s, W_{gpl}=0.1%, Foam-II, h=0.4 m, L=R=2 m, Ω=500 rad/s) and (b) spinning velocity (W_1=0.1, e_1=0.1, GPL-A, V_0 =240 m/s, W_{gpl}=0.1%, Foam-II, h=0.4 m, L=R=2 m, ΔT=150 K)

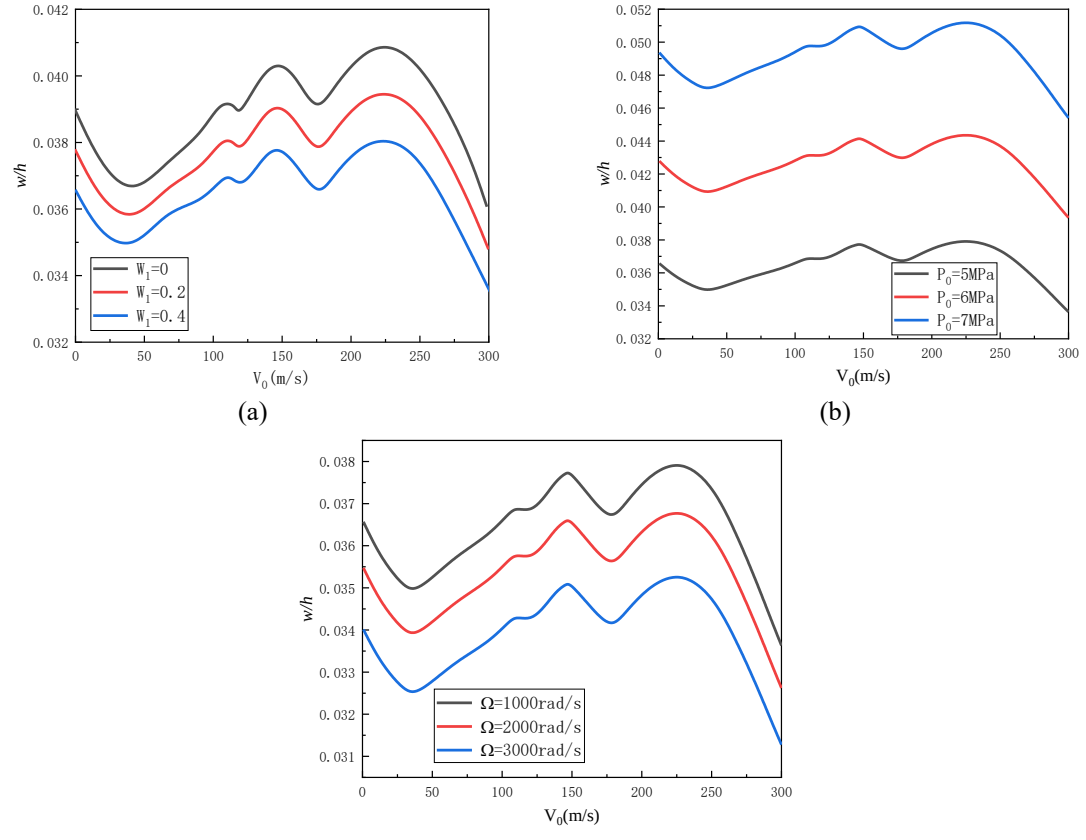

(a) (b)

(c)

Fig. 8 (a) Effect of W_1 (ΔT=150 K, e_1=0.1, GPL-A, W_{gpl}=0.1%, Foam-II, h=0.4 m, L=R=2 m, Ω=500 rad/s); (b) Effect of P_0 (ΔT=150 K, e_1=0.1, GPL-A, W_{gpl}=0.1%, Foam-II, h=0.4 m, L=R=2 m, Ω=500 rad/s); (c) Influence of spinning velocity (W_1=0.1, e_1=0.1, GPL-A, V_0=240 m/s, W_{gpl}=0.1%, Foam-II, h=0.4 m, L=R=2 m, ΔT=150 K)

under dynamic loading conditions.

Fig. 8(a) illustrates the impact of geometric imperfections on the peak deflection observed at the center of cylindrical shells. The data shows a consistent reduction in dynamic deflection as the magnitude of the imperfection grows. This occurs because the imperfections examined, being positive in value, enhance the shell's curvature, leading to an increase in structural rigidity. Furthermore, with increasing loading velocity (V_0), the deflection response initially shows small-amplitude oscillations at lower velocities. This oscillation amplitude then progressively intensifies, reaching a maximum before undergoing a sharp decline. This behavior stems from the shell's enhanced ability to constrain transverse deformations when subjected to loads at relatively slower speeds. The observed extremum points in the (w/h) variation curve correspond to critical transitions in energy transfer mechanisms. At lower loading velocities (V_0<15 m/s), the shell's enhanced rigidity suppresses transverse deformations, leading to small-amplitude oscillations. The maximum deflection peak at V_0≈15 m/s marks the resonance condition where the loading frequency matches the shell's natural frequency, resulting in optimal energy transfer from the load to the structure. Beyond this point, the sharp decline in displacement indicates the onset of dynamic instability, where stress wave propagation dominates over elastic deformation, causing rapid energy dissipation. This behavior aligns with classical shell theory predictions for bifurcation points in dynamic loading scenarios. Fig. 8(b) investigates the influence of P_0 on the peak deflection at the center of the cylindrical shell under different loading speeds. The results show that an increased load magnitude consistently leads to greater maximum deflection, which is attributed to the amplified kinetic energy transferred to the shell structure under heavy loading conditions. This is an expected outcome, as a larger external force will naturally produce greater displacement. Fig. 8(c) explores the role of rotational speed variations. The same findings confirm that higher rotational speeds result in smaller dynamic displacement responses. The monotonic displacement reduction in Fig. 10 (Ω=1000 rad/s) is attributed to gyroscopic stiffening induced by Coriolis forces. The absence of distinct extremum points suggests a stable energy transfer regime where rotating kinetic energy suppresses transverse vibrations. However, the inflection points at Ω=3000 rad/s marks the onset of gyroscopic dominance, where axial pre-stress increases structural stiffness by ~28%. This transition delineates the stability boundary of rotating shells beyond which transverse deformations become negligible.

5. Conclusions

The parametric study on graphene platelet (GPL)-reinforced cylindrical shells reveals critical insights into dynamic response optimization. The research demonstrates that GPL distribution patterns significantly influence structural performance, with surface-concentrated configurations (GPL-A) exhibiting superior deflection resistance during forced vibrations due to enhanced stiffness mechanisms. However, this advantage diminishes in free vibration regimes, suggesting distinct design criteria for transient versus steady-state conditions.

(1) Foam core topology emerges as another pivotal factor, with mid-plane concentrated distributions (Foam-I) demonstrating optimal flexural rigidity by enabling efficient stress redistribution compared to surface-localized foam arrangements. The study further establishes that foam coefficient variations exhibit differential sensitivity between forced and free vibration phases, highlighting the need for material architecture optimization based on specific loading conditions.

(2) Notably, the investigation uncovers complex coupling effects between load parameters and structural characteristics. While increasing load intensity consistently amplifies deflection, elevating loading velocity reveals phase-dependent behaviors with more pronounced effects in free vibration regimes. Temperature variations demonstrate counterintuitive deflection suppression effects, potentially attributable to thermal stress redistribution. The rotational speed analysis introduces an additional dimension, where centrifugal forces induce unexpected stiffness enhancement through pre-stress mechanisms.

These findings collectively suggest that multi-parameter optimization is essential for dynamic structural design. The research advocates for a synergistic approach considering GPL patterning, foam topology, and operational parameters (loading conditions, temperature, rotation) to achieve balanced performance across different vibration regimes. The study provides foundational principles for engineering applications requiring impact resistance and dynamic stability, while acknowledging the need for further exploration into nonlinear interaction effects between these variables.

Acknowledgement

The funding of Natural Science Foundation of Hunan Province (2024JJ8109); Scientific research project of Hunan Provincial Department of Education (24B0974 and 22B0956); Xiangtan science and technology planning project (CG-YB20240004) are acknowledged.

References

Abouelregal, A.E. (2022), "Modeling and analysis of a thermoviscoelastic rotating micro-scale beam under laser heat models of", *Thin Wall. Struct.*, **174**, 109150. https://doi.org/10.1016/j.tws.2022.109150.

Abouelregal, A.E. (2024), "Effect of non-local modified couple stress theory on the responses of axially moving thermoelastic nano-beams", *ZAMM-Zeitschrift fur Angewandte Mathematik und Mechanik*, **104**(4), 1-22. https://doi.org/10.1002/zamm.202200233.

Abouelregal, A.E., Akgoz, B. and Civalek, O. (2022), "Nonlocal thermoelastic vibration of a solid medium subjected to a pulsed heat flux via Caputo-Fabrizio fractional derivative heat conduction", *Appl. Phys. A*, **128**(8), 660. https://doi.org/10.1007/s00339-022-05786-5.

Baakeel, F., Eltaher, M.A., Basha, M.A., Melibari, A. and Abdelrhman, A.A. (2023), "Static and modal analysis of bio-inspired laminated composite shells using numerical simulation", *Adv. Aircraft Spacecraft Sci.*, **10**(4), 347-368. https://doi.org/10.12989/aas.2023.10.4.347.

Chai, Q.D., Wang, Y.Q. and Yang, F.L. (2023), "Frequency response of spinning cylindrical shells with discontinuous conditions: A semi method", *Thin Wall. Struct.*, **182**(A), 110253. https://doi.org/10.1016/j.tws.2022.110253.

Cheng, Y.H. and She, G.L. (2025), "Nonlinear dynamics of rotating graphene-reinforced composite blades under 1:2 internal resonance in fluid-submergeddmdd environments", *Ocean Eng.*, **341**(4), 122717. https://doi.org/10.1016/j.oceaneng.2025.122717.

Cheng, Y.H., She, G.L. and Eltaher, M.A. (2025), "Nonlinear internal resonance of graphene-reinforced metal foam plates with initial geometric imperfection under non-uniform temperature field", *Aerosp. Sci. Technol.*, **165**, 110491. https://doi.org/10.1016/j.ast.2025.110491.

Civalek, O. and Akgoz, B. (2025), "Size-dependent stability of embedded beams with variable cross section", *Int. J. Eng. Sci.*, **208**, 104210. https://doi.org/10.1016/j.ijengsci.2024.104210.

Dong, Y.H., Li, X.Y., Gao, K., Li, Y.H. and Yang, J. (2020), "Harmonic resonances of graphene-reinforced

nonlinear cylindrical shells: Effects of spinning motion and thermal environment", *Nonlin. Dyn.*, **99**(2), 981-1000. https://doi.org/10.1007/s11071-019-05297-8.

Ebrahimi, F. and Salari, E. (2015), "Nonlocal thermo-mechanical vibration analysis of functionally graded nanobeams in thermal environment", *Acta Astronautica*, **113**, 29-50. https://doi.org/10.1016/j.actaastro.2015.03.031.

Esmaeili, H.R. and Kiani, Y. (2022), "On the response of graphene platelet reinforced composite laminated plates subjected to instantaneous thermal shock", *Eng. Anal. Bound. Elem.*, **141**, 167-180. https://doi.org/10.1016/j.enganabound.2022.05.017.

Eyvazian, A., Shahsavari, D. and Karami, B. (2020), "On the dynamic of graphene reinforced nanocomposite cylindrical shells subjected to a moving harmonic load", *Int. J. Eng. Sci.*, **154**, 103339. https://doi.org/10.1016/j.ijengsci.2020.103339.

Fan, Y.H. and She, G.L. (2026), "Low-velocity impact response of rotating 2D-FGM annular plates with variable thickness", *Commun. Nonlin. Sci. Numer. Simul.*, **152**(Part D), 109373. https://doi.org/10.1016/j.cnsns.2025.109373.

Fan, Y.H., She, G.L. and Eltaher, M.A. (2025), "Nonlinear vibrations of two-directional functionally graded spinning annular plates with variable thickness", *Thin Wall. Struct.*, **216**(A), 113627. https://doi.org/10.1016/j.tws.2025.113627.

Gao, G.H., Sun, N.Z., Shao, D., Tao, Y.Q. and Zhang, H. (2024), "Nonstationary response system for the stepped composite cylindrical shell with drop-off ply under moving random loads", *Ocean Eng.*, **298**, 117178. https://doi.org/10.1016/j.oceaneng.2024.117178.

Goudarzfallahi, M., Ziazi, A.A. and Ebrahimi, F. (2025), "Third-order shear deformable porous metamaterial toroidal shells with arc-type auxetic core: A stability analysis", *Adv. Aircraft Spacecraft Sci.*, **12**(2), 177-195. https://doi.org/10.12989/aas.2025.12.2.177.

Jafari, P. and Kiani, Y. (2022a), "A four-variable shear and normal deformable quasi-3D beam model to analyze the free and forced vibrations of FG-GPLRC beams under moving load", *Acta Mechanica*, **233**(7), 2797-2814. https://doi.org/10.1007/s00707-022-03256-w.

Jafari, P. and Kiani, Y. (2022b), "Analysis of arbitrary thick graphene platelet reinforced composite plates subjected to moving load using a shear and normal deformable plate model", *Mater. Today Commun.*, **31**, 103745. https://doi.org/10.1016/j.mtcomm.2022.103745.

Javani, M., Kiani, Y. and Eslami, M.R. (2021), "Free vibration analysis of FG-GPLRC L-shaped plates implementing GDQE approach", *Thin Wall. Struct.*, **162**, 107600. https://doi.org/10.1016/j.tws.2021.107600.

Javani, M., Kiani, Y. and Eslami, M.R. (2022), "On the free vibrations of FG-GPLRC folded plates using GDQE procedure", *Compos. Struct.*, **286**, 115273. https://doi.org/10.1016/j.compstruct.2022.115273.

Kiani, Y. and Eslamic, M.R. (2013), "An exact solution for thermal buckling of annular FGM plates on an elastic medium", *Compos. Part B-Eng.*, **45**(1), 101-110. https://doi.org/10.1016/j.compositesb.2012.09.034.

Kiani, Y. and Mirzaei, M. (2019), "Isogeometric thermal postbuckling of FG-GPLRC laminated plates", *Steel Compos. Struct.*, **32**(6), 821-832. https://doi.org/10.12989/scs.2019.32.6.821.

Li, Y.P. and She, G.L. (2025), "Nonlinear dynamic response of graphene platelets reinforced cylindrical shells under moving loads considering initial geometric imperfection", *Eng. Struct.*, **323**(A), 119241. https://doi.org/10.1016/j.engstruct.2024.119241.

Li, Z., Wang, Q.S., Yang, Q. and Qin, B. (2025), "Stochastic vibration behaviors of functionally graded graphene platelets reinforced composite joined conical-cylindrical-conical shell with variable taper under moving random loads", *Compos. Struct.*, **358**, 118970. https://doi.org/10.1016/j.compstruct.2025.118970.

Liu, H., Dong, Y.H., Wang, L.F. and Hu, H.Y. (2023), "Travelling-modes of a spinning cylindrical shell with elastic boundaries", *Int. J. Mech. Sci.*, **238**, 107844. https://doi.org/10.1016/j.ijmecsci.2022.107844.

Malekzadeh, P., Fiouz, A.R. and Razi, H. (2009), "Three-dimensional dynamic analysis of laminated composite plates subjected to moving load", *Compos. Struct.*, **90**(2), 105-114. https://doi.org/10.1016/j.compstruct.2009.02.008.

Meksi, A., Draiche, K., Madenci, E. and Tounsi, A. (2025), "A new higher-order displacement model for

laminated composite cylindrical shells", *Adv. Aircraft Spacecraft Sci.*, **12**(2), 117-139. https://doi.org/10.12989/aas.2025.12.2.117.

Mirjavadi, S.S., Forsat, M., Barati, M.R., Abdella, G.M., Afshari, B.M., Hamouda, A.M.S. and Rabby, S. (2019), "Dynamic response of metal foam FG porous cylindrical micro-shells due to moving loads with strain gradient size-dependency", *Eur. Phys. J. Plus*, **134**(5), 214. https://doi.org/10.1140/epjp/i2019-12540-3.

Mirzaei, M. and Abbasi, M. (2023), "Dynamic response of moderately thick graphene reinforced composite cylindrical panels under the action of moving load", *Eng. Anal. Bound. Elem.*, **146**, 292-305. https://doi.org/10.1016/j.enganabound.2022.10.032.

Mohamed, N., Mohamed, S.A. and Eltaher, M.A. (2024), "Exact solutions of vibration and postbuckling response of curved beam rested on nonlinear viscoelastic foundations", *Adv. Aircraft Spacecraft Sci.*, **11**, 55-81. https://doi.org/10.12989/aas.2024.11.1.055.

Monajemi, A.A., Mohammadimehr, M. and Bargozini, F. (2024), "Dynamic analysis of a spinning visco-elastic FG graphene platelets reinforced nanocomposite sandwich cylindrical shell with MRE core*", Acta Mechanica*, **235**(12), 7497-7530. https://doi.org/10.1007/s00707-024-04077-9.

Rafiee, M., Rafiee, J., Wang, Z., Song, H.H., Yu, Z.Z. and Koratkar, N. (2009), "Enhanced mechanical properties of nanocomposites at low graphene content", *ACS Nano*, **3**(12), 3884-3890. https://doi.org/10.1021/nn9010472.

Salehi, M., Gholami, R. and Ansari, R. (2023), "Analytical solution approach for nonlinear vibration of shear deformable imperfect FG-GPLR porous nanocomposite cylindrical shells", *Mech. Bas. Des. Struct. Mach.*, **51**(4), 2177-2199. https://doi.org/10.1080/15397734.2021.1891096.

Sheng, G.G. and Wang, X. (2009), "Studies on dynamic behavior of functionally graded cylindrical shells with PZT layers under moving loads", *J. Sound Vib.*, **323**(3-5), 772-789. https://doi.org/10.1016/j.jsv.2009.01.017.

Sofiyev, A.H. (2010), "Dynamic response of an FGM cylindrical shell under moving loads", *Compos. Struct.*, **93**(1), 58-66. https://doi.org/10.1016/j.compstruct.2010.06.015.

Sofiyev, A.H., Halilov, H.M. and Kuruoglu, N. (2011), "Analytical solution of the dynamic behavior of non-homogenous orthotropic cylindrical shells on elastic foundations under moving loads", *J. Eng. Math.*, **69**(4), 359-371. https://doi.org/10.1007/s10665-010-9392-x.

Teng, N.W. and Wang, Y.Q. (2023), "Thickness configuration effect on frequency and critical speed of spinning variable-thickness cylindrical shells", *Int. J. Struct. Stab. Dyn.*, **23**(05), 1-20. https://doi.org/10.1142/S0219455423500554.

Wang, Y.X. and Kiani, Y. (2022), "Effects of initial compression/tension, foundation damping and pasternak medium on the dynamics of shear and normal deformable GPLRC beams under moving load", *Mater. Today Commun.*, **33**(1), 104938. https://doi.org/10.1016/j.mtcomm.2022.104938.

Zhang, C.H., Chai, Q.D. and Wang, Y.Q. (2025), "Free vibration of spinning stepped functionally graded circular cylindrical shells in a thermal environment", *Mech. Bas. Des. Struct. Mach.*, **53**(3), 2075-2092. https://doi.org/10.1080/15397734.2024.2402390.

Zhang, W., Ma, H., Wang, Y.B. and Wang, Y.W. (2023), "Nonlinear transient thermo-mechanical responses of porous graphene platelet-reinforced cylindrical panels under moving distributed loads", *Thin Wall. Struct*., **192**, https://doi.org/111180. 10.1016/j.tws.2023.111180.

Zhang, Y., Xu, H.D., Wang, Y., Liu, H.R. and Zhang, Y.F. (2024), "Semi-analytical modeling and analysis on traveling wave vibration characteristics of spinning FGP-GPLRC stepped cylindrical shells under discontinuous boundary conditions", *Arch. Appl. Mech.*, **94**(10), 2989-3015. https://doi.org/10.1007/s00419-024-02654-x.

Zhao, B. and She, G.L. (2025), "Vibration analysis of graphene reinforced metal foam coupled plates under arbitrary boundary and coupled conditions", *Eng. Struct.*, **343**(C), 121143. https://doi.org/10.1016/j.engstruct.2025.121143.

Zhao, B., Eltaher, M.A. and She, G.L. (2025), "Dynamic response analysis of acoustic black hole plates with cutouts under arbitrary boundary constraints", *Thin Wall. Struct.*, **217**(Part A), 113859. https://doi.org/10.1016/j.tws.2025.113859.

Zhao, T.Y., Yan, K., Chen, L. and Wang, X. (2023), "Vibration analysis of spinning porous cylindrical shell coupled with multiple plates assembly structures reinforced by graphene nanoplatelets", *Thin Wall. Struct*., **184**, 110498. https://doi.org/10.1016/j.tws.2022.110498.

Zhao, T.Y., Yan, K., Jiang, Z.Y. and Chi, W.C. (2024), "Theoretical modeling and vibration prediction of a spinning graphene nanoplatelet reinforced cylindrical shell internal attached with a beam", *Mech. Bas. Des. Struct. Mach.*, **52**(4), 2297-2315. https://doi.org/10.1080/15397734.2023.2177862.

CC